The Astrophysical Journal Letters, 773:L30 (5pp), 2013 August 20 doi:10.1088/2041-8205/773/2/L30

PREDICTION OF TYPE II SOLAR RADIO BURSTS BY THREE-DIMENSIONAL MHD CORONAL MASS EJECTION AND KINETIC RADIO EMISSION SIMULATIONS

J. M. Schmidt[1], Iver H. Cairns[1], and D. S. Hillan[2]
[1] School of Physics, University of Sydney, NSW 2006, Australia; jschmidt@physics.usyd.edu.au
[2] CSIRO Earth Science and Resource Engineering, North Ryde, NSW 2113, Australia
Received 2013 June 16; accepted 2013 July 14; published 2013 August 6

ABSTRACT

Type II solar radio bursts are the primary radio emissions generated by shocks and they are linked with impending space weather events at Earth. We simulate type II bursts by combining elaborate three-dimensional MHD simulations of realistic coronal mass ejections (CMEs) at the Sun with an analytic kinetic radiation theory developed recently. The modeling includes initialization with solar magnetic and active region fields reconstructed from magnetograms of the Sun, a flux rope of the initial CME dimensioned with *STEREO* spacecraft observations, and a solar wind driven with averaged empirical data. We demonstrate impressive accuracy in time, frequency, and intensity for the CME and type II burst observed on 2011 February 15. This implies real understanding of the physical processes involved regarding the radio emission excitation by shocks and supports the near-term development of a capability to predict and track these events for space weather prediction.

Key words: solar-terrestrial relations – Sun: coronal mass ejections (CMEs) – Sun: radio radiation

Online-only material: color figures

1. INTRODUCTION

Coronal mass ejections (CMEs) are major solar transient events. CMEs and their shock waves, fast and dense plasma flows, and large and changing magnetic fields are associated with almost 90% of large space weather events at Earth (Richardson et al. 2006). These events include geo-magnetic storms and related disruptions to electrical power grids due to large induced voltages and currents, solar and magnetospheric energetic particle events that damage spacecraft systems and degrade data, and changing ionospheric conditions that disrupt communications and GPS. Observed with coronagraph and in situ spacecraft measurements, CMEs carry mass, momentum, and magnetic flux away from the Sun (Hundhausen 1999). Measured CME speeds range from less than 100 to 3000 km s^{-1}, with estimated masses as large as 10^{13} kg (Gopalswamy 2006; St. Cyr et al. 2000; Hundhausen 1999). Large CMEs can drive a shock when moving faster than the local fast mode speed. Such shocks can produce type II radio bursts by accelerating the electrons. Accurate simulation of type II radio bursts not only addresses the fundamental shock and radio emission physics, but also provides the predictive power necessary to establish whether type II radio bursts provide reliable warnings of the large and fast CMEs that drive large space weather events. If so, then iterative data–theory comparison may allow extraction of the time-varying CME position and velocity, thereby allowing prediction of whether the CME will hit Earth's magnetosphere and cause significant space weather effects. This Letter demonstrates excellent agreement between theory, simulation, and observation for the type II burst and CME of 2011 February 15, the strongest type II radio burst and one of the largest Earth-directed CMEs in the previous four years and precursors to multiple days of strong space weather activity (http://www.swpc.noaa.gov/weekly/2011_WeeklyPDF/prf1851.pdf). As well as strongly supporting the related type II theory and CME simulation capability, this points toward a near-term capability to extract CME properties from radio data and predict space weather at Earth and elsewhere.

Type II radio bursts, the Sun's second most intense class of metric emissions, often occur in two bursty time-varying bands differing by a factor of two in frequency (Lengyel-Frey et al. 1997; Nelson & Melrose 1985; Cane et al. 1981; Wild & Smerd 1972). Their slow frequency drift rate, from 200 MHz to 30 MHz in about 5 minutes in the corona, and in the solar wind from 30 MHz to 30 kHz in 1–3 days, is interpreted in terms of radio emission near the electron plasma frequency f_p (f_p^2 is proportional to the electron number density n_e) and near $2f_p$ associated with a propagating shock wave. Type IIs are closely correlated with shocks ahead of CMEs, although blast wave shocks caused by flares may sometimes be relevant. Very strong evidence exists for interplanetary type IIs (Cairns 2011; Pulupa et al. 2010; Mann & Klassen 2005; Reiner & Kaiser 1999; Bale et al. 1999; Reiner et al. 1998, 1997; Cane et al. 1981) that (1) the radio emission is generated near f_p and near $2f_p$ upstream of the shock and (2) the foreshock region upstream of a CME-driven shock that emits type II radiation contains Langmuir waves and electron beams.

Type II bursts are the archetype for collective radio emission associated with shock waves. They involve fundamental plasma physics in four main steps (Cairns 2011; Mann & Klassen 2005; Nelson & Melrose 1985): (1) electron acceleration near or at the shock; (2) formation of beam distributions of accelerated electrons upstream of the shock; (3) generation of high levels of Langmuir waves via electron beam instabilities; and (4) production of f_p and $2f_p$ emission via linear and nonlinear Langmuir wave processes, leading to the observed type II burst. Testing each step is important, as are applications of the archetypal theory to radiation from upstream of Earth's bow shock (Kuncic et al. 2002), 2–3 kHz radiation from near the heliopause (Mitchell et al. 2004), drifting pulsating structures in the deep corona (Karlicky 2003), and collective emission from shocks associated with supernova, nova, and astrospheres.

This Letter provides a first detailed quantitative test of state-of-the-art type II theory with event-specific three-dimensional (3D) CME and shock predictions. We combine the radio theory developed at the University of Sydney (Schmidt & Cairns 2012a,

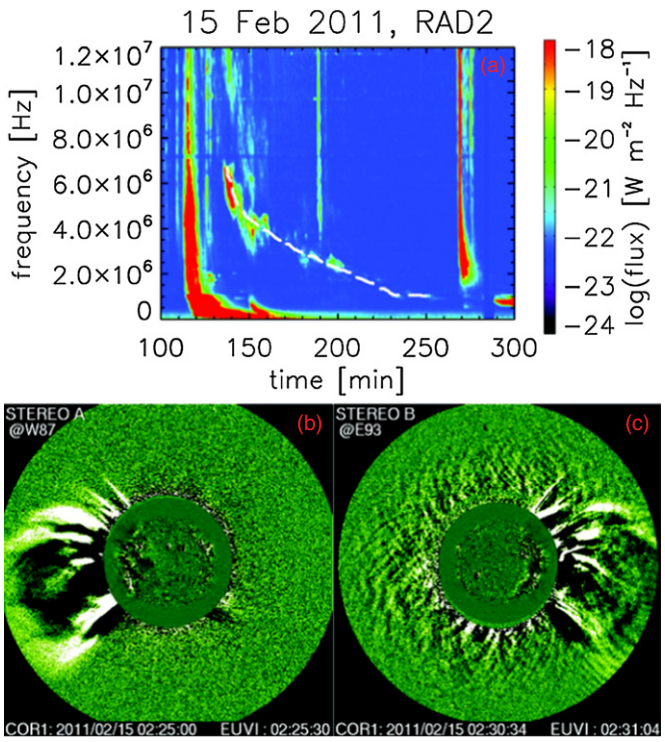

Figure 1. (a) Type II radio burst observed by the *WIND* spacecraft on 2011 February 15 UT (the bursty hyperbolic band indicated with a white dashed line). Most of the almost vertical streaks are type III bursts. (b) and (c): *STEREO A* (*B*) coronagraph observation of the erupting flux rope of a halo CME on 2011 February 15 2:25 (2:30) UT.

(A color version of this figure is available in the online journal.)

2012b; Florens et al. 2007; Cairns & Knock 2006; Knock & Cairns 2005; Knock et al. 2001, 2003a, 2003b) with the University of Michigan's BATS-R-US MHD code (Roussev et al. 2003, 2004) for the 2011 February 15 type II and CME. This Letter leverages data from multiple ground (Wilcox, Learmonth) and space (*ACE*, *STEREO*, *WIND*) platforms to develop detailed BATS-R-US models for the background corona and CME initiation and to test the ensuing predictions for the CME and radio emission.

2. TYPE II RADIO BURST AND CME OBSERVATIONS

On 2011 February 15, a type II radio burst was detected with the WAVES experiment on the *WIND* spacecraft in Earth orbit (see http://ssed.gsfc.nasa.gov/waves/). This experiment consists of five receivers, TDS, FFT, TNR, RAD1, and RAD2, measuring in adjacent frequency bands between DC and 13.825 MHz. Figure 1(a) shows the calibrated *WIND* measurements (1 minute averages) of RAD2 in the frequency range between 1 MHz and 12 MHz for the time interval 100–300 minutes on 2011 February 15 UT. The radio signals are displayed as color-coded contours with fluxes between 10^{-22} Wm^{-2} Hz^{-1} and 10^{-18} Wm^{-2} Hz^{-1}, where the background level is 10^{-22} Wm^{-2} Hz^{-1}. The type II radio burst occurred early on 2011 February 15: it is the bursty signal that follows the approximately hyperbolic line starting at 7.0×10^6 Hz around 140 minutes and ending at 1.0×10^6 Hz around 250 minutes. This radiation is interpreted as fundamental emission near f_p.

The corresponding strong halo CME event, which drives the type II radio burst and hits the Earth, was observed with the two *STEREO A* (*B*) spacecraft (http://cdaw.gsfc.nasa.gov/CME_list/). The *STEREO A* and *B* spacecraft move ahead of and behind Earth in its orbit at 1 AU, respectively, each carrying COR1 and COR2 coronagraphs (Kaiser et al. 2008; Howard et al. 2008). The COR1 coronagraphs measure at a distinct spectral line of wavelength 656 nm. Figures 1(b) and (c) show *STEREO A* (*B*) COR1 difference images of 2011 February 15 near 2:25 (2:30) UT, where the cross section of the magnetic flux rope of the CME is the rounded distortion on the left (right) side of the images. Triangulation of the *STEREO A*/*B* coronagraph images leads to a CME speed of 669 km s^{-1} (http://cdaw.gsfc.nasa.gov/CME_list/). The *STEREO* COR1 images can also be used to determine the radius, diameter, height above the solar surface, and the orientation of the erupting flux rope of the CME at a given initial time.

STEREO/WAVES also observes this event. Only *WIND* data–theory comparisons are presented here since these minimize propagation effects.

3. MHD MODEL OF THE CME

The fully parallelized BATS-R-US code (Roussev et al. 2003, 2004), which uses adaptive mesh refinement, is used for the 3D solution of the complete set of resistive MHD equations. It has a Riemann-solver-based algorithm on a Cartesian computational grid for the computation of time-dependent fluxes between cubic cells. Initially, BATS-R-US achieves a realistic 3D reconstruction of the complete 3D solar corona. This provides an environment for launching a CME, including, e.g., an active region, streamers, and a magnetic field arcades network.

A photospheric magnetogram of an appropriate Carrington rotation of the Sun is used for the initial setup of the code. This enables a reconstruction of the 3D solar corona magnetic fields using an extrapolation of the solar surface source potential field. At a specific time, the reconstructed fields can be adjusted to observations of the Sun using ground-based magnetogram data of Wilcox Solar Observatory for Carrington rotation ⟨2105⟩. In general, the reconstructed magnetic field consists of a streamer belt, one ore more active regions, and coronal holes. On 2011 February 15, an active region occurred at 30° longitude and 20° latitude north, which is the location of the CME outburst that followed near 2 UT.

The BATS-R-US (version 9) code used has a refined solar wind model driven with empirical data (Cohen et al. 2008). The initial solar wind in BATS-R-US is a plasma with acceleration away from the Sun. This acceleration is generated with empirical heating functions that mimic wave energy dissipation or magnetic reconnection induced release of magnetic energy. Spatially varying empirical polytropic indices address a solar wind that can expand non-adiabatically.

The initial CME is a Titov and Démoulin type bent flux rope (Titov & Démoulin 1999). A current of 1.1×10^{12} ampere parallel to the solar surface generates that loop, which extends above the simulated active region. This loop has a twisted flux rope structure with a decreasing magnetic helicity from the rope's boundary to the rope's middle axis. The loop's initial density is larger than that outside. This creates a steady state for the loop, where gravitational forces acting on the loop compensate outward-driving thermal pressure and magnetic buoyancy. 1.0×10^{13} kg is the simulated mass of the loop. Radial stretching can give the loop a teardrop shape. Speed observations of large eruption radial speeds can be matched with increased stretching.

STEREO coronagraph observations yield an initial aspect ratio of 0.8 between the loop cross section's minor and major

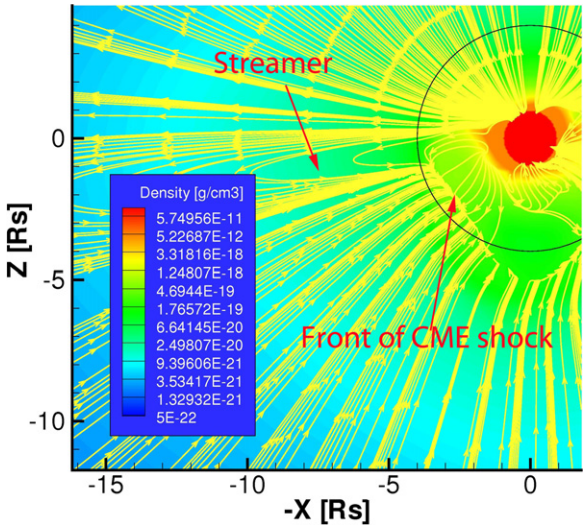

Figure 2. Magnetic fields (yellow lines) and density (color contours) for the 2011 February 15 CME driving a shock front and interacting with a streamer, as simulated with the BATS-R-US code. The plane shown is perpendicular to the ecliptic and includes the Sun as a red dot and the Earth in the *X*-direction. The black circle is the field of view of *STEREO*/COR1.

(A color version of this figure is available in the online journal.)

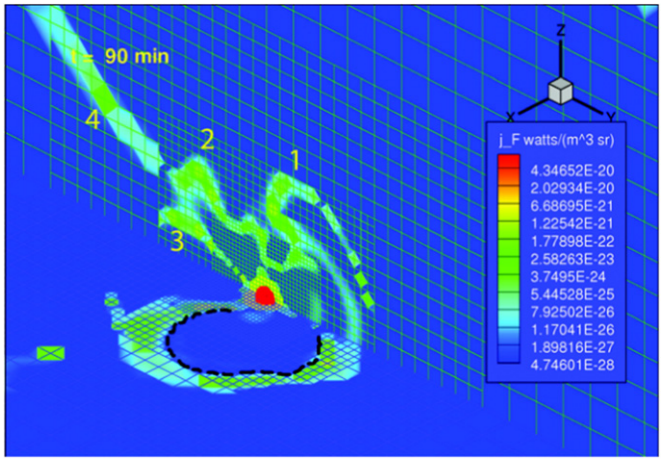

Figure 3. Fundamental emissivity j_F upstream of the CME-driven shock as contour plots in the X–Y and Y–Z planes, 90 minutes (230 minutes UT on 2011 February 15) after the initiation of the CME. Here X is the direction toward the Earth and Z the rotation axis of the Sun. The Sun is the red dot in the center. The majority of the radiation is in the half-moon shaped area upstream of the CME-driven shock represented with the black dashed line. There are further radio sources (e.g., 1–4) that stem from interactions of the CME with the corotating interaction regions of the Sun, which are misinterpreted as shock fronts.

(A color version of this figure is available in the online journal.)

axes. The major axis is 9.0×10^6 m. *STEREO* coronagraph observations are used to specify 1.5×10^7 m as the distance between the initial flux rope's center and the Sun's surface, 6.0×10^7 m as the flux rope's initial radius, and zero as the tilt angle between the axis of the flux rope and the ecliptic plane. The Titov and Démoulin flux rope also has a dipolar electric field, which dipole vector is perpendicular to the loop's plane. The dipole charge is 2.39×10^{13} C separated by 6.0×10^7 m; these are typical values for the solar corona.

Dense plasma outflowing from the flux rope triggers the eruption. In addition, below the rope a pressure pulse is generated, which velocity shear signal cancels magnetic flux. This severs magnetic field lines tying the solar surface with the flux rope. Both effects cause the eruption of the CME.

After initiation, the CME evolves in a simulation cube with a side length of 48 solar radii (R_s), where the Sun is a spherical cavity of radius 1 R_s in the middle of this box. Figure 2 shows the CME in the X–Z plane shortly after initiation, where the X-axis connects the Earth with the Sun at the origin, and the Z-axis is the Sun's rotation axis. Projections of the 3D magnetic field lines onto that plane are shown as yellow lines, where the arrows indicate the field direction. The Sun is represented as a red dot. Color-coded contours of the plasma density provide the background image. The cavity of the CME can be discerned southwest of the Sun with a density of 1.7×10^{-19} g cm^{-3}. The front of the CME's shock can be identified at the southwestern edge, where the projections of the external radial magnetic field lines of the Sun end. The image also reveals a coronal streamer with a magnetic loop extending roughly in the western direction. The black circle in the image has the size of *STEREO*'s COR1 coronagraph field of view.

4. CALCULATION OF THE RADIO EMISSION

The computed MHD fields are extracted from the simulation box in order to calculate the properties of the CME-driven shock. In particular, the gradient of the entropy is used to determine the shock's location, which is a surface of constant entropy. This gradient is maximum at the location of the shock and is normal to the shock's surface. With the shock normal given, the angle θ_{bn} between the magnetic field direction and the shock normal and the upstream velocity of the plasma up streaming the shock can be calculated. Both are important parameters that determine how effectively the shock can accelerate electrons. Further parameters that determine the effectiveness of the electron acceleration at the shock, like the cross-shock potential and the electron temperature, are calculated using the MHD fields and the Rankine–Hugoniot conditions. These parameters then enter the analytic formulae for the plasma emissivities that are derived in detail in Schmidt & Cairns (2012a, 2012b).

The initial grid resolution of the BATS-R-US code is $1/24 R_s$ before adaptive mesh refinement starts. Combining the shock speed of 669 km s^{-1} with the 1 minute radio sampling implies an effective spatial resolution of $1/18 R_s$. Thus the code easily resolves shock structures $\sim 10^9$ m $\approx 1 R_s$ observed at 1 AU (Bale et al. 1999; Knock et al. 2003a; Pulupa et al. 2010).

Figure 3 shows the resulting power emitted per unit volume near the local plasma frequency (the emissivity j_F) 90 minutes after shock initiation. The figure displays j_F as color-coded contour plots in the X–Y and Y–Z planes defined above. The radiation is calculated at locations starting just upstream of the shock and then along trajectories of the reflected electron beams. In this way the radiation field upstream of the shock can be mapped. The majority of the radiation is in a half-moon shaped area upstream from the CME-driven shock; this domain expands with the shock along the X-direction with increasing time. An arc-like extension of this domain can be seen in the first quadrant of the Y–Z plane. However, the intensity of this arc-like source is smaller than the intensity of the crescent in the X–Y plane, since it is moving more slowly and is closer to the rear of the CME. In the half-moon shaped radio source moving in front of the shock there are regions with j_F up to 10^{-21} Wm^{-3} sr^{-1}, whereas the emissivity nearer the shock's nose (furthest from the Sun) is near 10^{-25} Wm^{-3} sr^{-1}. The intensity enhancements toward the side of the shock are associated with ripples on the shock surface (Hillan et al. 2012a, 2012b), where the shock

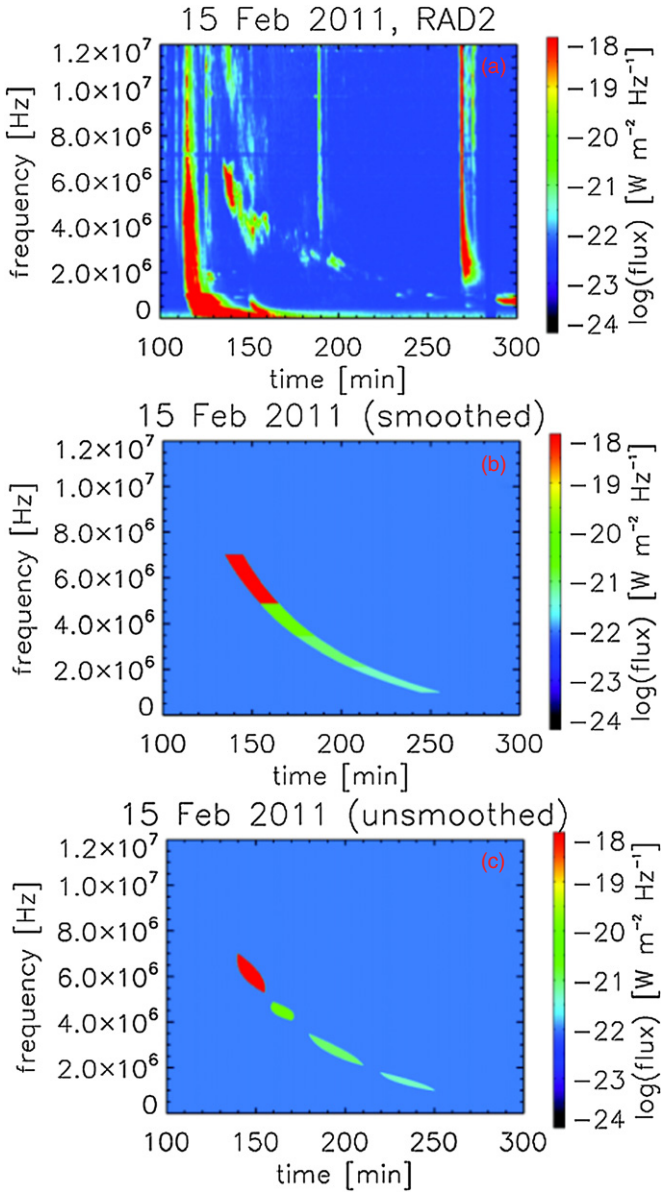

Figure 4. (a) The *WIND* type II radio burst data of 2011 February 15 and the theoretical predictions for the type II burst assuming that the CME shock moves through a (b) smoothed and (c) unsmoothed plasma background.

(A color version of this figure is available in the online journal.)

becomes more quasi-perpendicular to the magnetic field and is thus more effective at accelerating electrons.

There are further apparent radio sources that stem from interactions of the CME with corotating interaction regions, which are misinterpreted as shock fronts by the entropy gradient method. These sources occur at more poleward locations in the current simulation.

For this CME the volume emissivity j_H emitted near $2f_p$ remains near the background level. Only fundamental radiation is thus discussed further below.

5. DISCUSSION OF COMPUTED DYNAMIC SPECTRA AND CONCLUSIONS

The BATS-R-US modeling of the time-varying solar coronal fields and the solar wind shows preexisting disturbances in the background plasma through which the CME-driven shock propagates. These disturbances are expected to modify the effectiveness of electron acceleration at the CME-driven shock and thus affect the radio dynamic spectrum. In order to avoid these effects, the MHD background fields in the Cartesian cells in the upstream region can be smoothed prior to the computation of the emissivities j_F and the dynamic spectrum. The source volume upstream the shock is covered with a Cartesian grid of about 3,000,000 cells. The dynamic spectrum, or radio flux as a function of frequency and time, is calculated by summing the emissivities from cells that emit in a specific frequency interval. These summations are carried out for neighboring frequency intervals that cover the complete frequency range and the entire volume upstream of the shock, where the decrease of the intensity with distance to an observer at Earth is taken into account. The measured frequency-dependent radio background of 10^{-22} Wm^{-2} Hz^{-1} for the *WIND* spacecraft is then added. These calculations are carried out at 25 time cuts during the simulation.

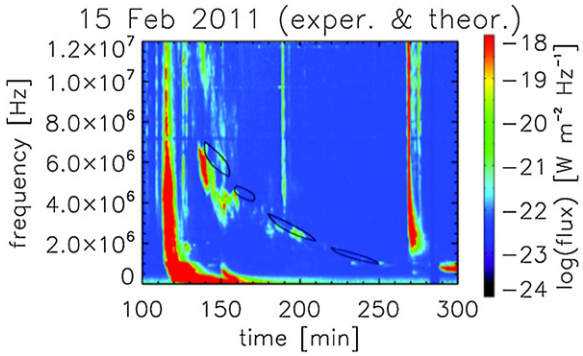

Figure 5. Comparison between the observed and the theoretical predictions for the type II radio burst on 2011 February 15. The theoretical bursts of type II radiation from Figure 4(c) are indicated with shapes bounded with a black line. They coincide very closely with the observed emission.

(A color version of this figure is available in the online journal.)

Figures 4(b) and (c) show the theoretical predictions for the simulated type II radio burst, while Figure 4(a) shows the *WIND* observations of Figure 1(a) for comparison. Figure 4(b) includes the smoothing of the background-density field. Radio fluxes are obtained in Figure 4(b) of 10^{-18} Wm^{-2} Hz^{-1} in the time interval between 140 minutes and 160 minutes, 10^{-20} Wm^{-2} Hz^{-1} between 160 minutes and 180 minutes, 10^{-21} Wm^{-2} Hz^{-1} between 180 minutes and 210 minutes, and 5×10^{-22} Wm^{-2} Hz^{-1} between 210 minutes and 250 minutes. These values agree well with the majority of the measured values in the same time intervals in Figure 4(a). In Figure 4(c) we display the theoretical radio type II burst of the simulation without prior smoothing of the MHD background-density fields. The four sections of the simulated radio burst emitting at 10^{-18} Wm^{-2} Hz^{-1}, 10^{-20} Wm^{-2} Hz^{-1}, 10^{-21} Wm^{-2} Hz^{-1}, and 5×10^{-22} Wm^{-2} Hz^{-1}, respectively, are now separated into islands of observable emission. The detailed time- and frequency-dependent structure of the theoretical predictions now corresponds very closely with the observed radio burst. Peak intensities in Figure 4(c) are larger than in Figure 4(b) in the center of the islands and smaller than in Figure 4(b) toward the edges, which means that coronal structures enhance and modulate the radio intensity.

Figure 5 shows the measured *WIND* data again but with the theoretical emission from Figure 4(c) overplotted as shapes bordered with a black line. These theoretical predictions coincide very closely with the observed emission in frequency and time.

The more ragged structure of the observed radio burst can be attributed to more fine structures (in space and time) in the real background fields, which the idealized simulation cannot resolve.

This study provides the first detailed test for the type II theory (Schmidt & Cairns 2012a, 2012b; Hillan et al. 2012a, 2012b; Florens et al. 2007; Cairns & Knock 2006; Knock et al. 2001, 2003a, 2003b) with state-of-the-art shock and CME simulations. Figures 2–5 demonstrate excellent quantitative agreement between theory and observations. This is a crucial demonstration that a detailed and accurate theory exists for type II bursts and a fundamental step toward using type II bursts to predict CME properties for space weather applications. This capability can now be used to simulate observed type II bursts and predict via future iterative data–theory comparisons (see Hillan et al. (2012a, 2012b) for pilot studies) which CMEs will reach Earth, when, what the solar wind and CME properties will be, and what space weather events the CME is likely to produce. Forewarning of 1 day appears viable, since CME travel times are ≈2–3 days, the BATS-R-US and radio emission predicting codes can be run faster than real time, and only ≈4 hr of radio data are used. Future work will determine how common such well-simulated events are. However, a similar analysis also yields excellent agreement with observations for the geo-effective CME and type II burst of 2012 March 7.

We acknowledge comments from D. B. Melrose, G. Tôth, B. Li, and V. L. Lobzin, and ARC funding. The SWMF/BATS-R-US codes were developed at The University of Michigan Center for Space Environment Modeling (CSEM) and made available through the NASA Community Coordinated Modeling Center (CCMC).

REFERENCES

Bale, S. D., Reiner, M. J., Bougeret, J.-L., et al. 1999, GeoRL, 26, 1573
Cairns, I. H. 2011, The Sun, the Solar Wind, and the Heliosphere (New York: Springer), 269
Cairns, I. H., & Knock, S. A. 2006, Planetary Radio Emissions VI Proceedings, ed. H. Rucker, W. Kurth, & G. Mann (Verlag: Ost. Akad. Wissenschaften), 419
Cane, H. V., Stone, R. G., Fainberg, J., et al. 1981, GeoRL, 8, 1285
Cohen, O., Sokolov, I. V., Roussev, I. I., & Gombosi, T. I. 2008, JGR, 113, 3104
Florens, M. S. L., Cairns, I. H., Knock, S. A., & Robinson, P. A. 2007, GeoRL, 34, 4104
Gopalswamy, N. 2006, J. Air Waste Manage. Assoc., 27, 243
Hillan, D. S., Cairns, I. H., & Robinson, P. A. 2012a, JGR, 117, 3104
Hillan, D. S., Cairns, I. H., & Robinson, P. A. 2012b, JGR, 117, 6105
Howard, R. A., Moses, J. D., Vourlidas, A., et al. 2008, SSRv, 136, 67
Hundhausen, A. J. 1999, The Many Faces of the Sun: A Summary of the Results From NASA's Solar Maximum Mission (New York: Springer), 143
Kaiser, M. L., Kucera, T. A., Davila, J. M., et al. 2008, SSRv, 136, 5
Karlicky, M. 2003, SSRv, 107, 81
Knock, S. A., & Cairns, I. H. 2005, JGR, 110, 1101
Knock, S. A., Cairns, I. H., & Robinson, P. A. 2003a, JGR, 108, 1361
Knock, S. A., Cairns, I. H., Robinson, P. A., & Kuncic, Z. 2001, JGR, 106, 25041
Knock, S. A., Cairns, I. H., Robinson, P. A., & Kuncic, Z. 2003b, JGR, 108, 1126
Kuncic, Z., Cairns, I. H., Knock, S. A., & Robinson, P. A. 2002, GeoRL, 29, 1161
Lengyel-Frey, D., Golla, T., MacDowall, R. J., Stone, R. G., & Philips, J. L. 1997, JGR, 102, 2611
Mann, G., & Klassen, A. 2005, A&A, 441, 319
Mitchell, J. J., Cairns, I. H., & Robinson, P. A. 2004, JGR, 109, 6108
Nelson, G. J., & Melrose, D. B. 1985, Solar Radiophysics: Studies of Emission From the Sun at Metre Wavelengths (New York: Cambridge Univ. Press), 333
Pulupa, M. P., Bale, S. D., & Kasper, J. C. 2010, JGR, 115, 4106
Reiner, M. J., & Kaiser, M. L. 1999, JGR, 104, 16979
Reiner, M. J., Kaiser, M. L., Fainberg, J., Bougeret, J. L., & Stone, R. G. 1997, in Proc. ESLAB Symp., vol. 415, Correlated Phenomena at the Sun, in the Heliosphere and in Geospace, ed. A. Wilson (Noordwijk: ESA), 183
Reiner, M. J., Kaiser, M. L., Fainberg, J., & Stone, R. G. 1998, JGR, 103, 29651
Richardson, I. G., Webb, D. F., Zhang, J., et al. 2006, JGR, 111, 7
Roussev, I. I., Gombosi, T. I., Sokolov, I. V., et al. 2003, ApJL, 595, L57
Roussev, I. I., Sokolov, I. V., Forbes, T. G., et al. 2004, ApJL, 605, L73
Schmidt, J. M., & Cairns, I. H. 2012a, JGR, 117, 4106
Schmidt, J. M., & Cairns, I. H. 2012b, JGR, 117, 11104
St. Cyr, O. C., Plunkett, S. P., Michels, D. J., et al. 2000, JGR, 105, 18169
Titov, V. S., & Démoulin, P. 1999, A&A, 351, 707
Wild, J. P., & Smerd, S. F. 1972, ARA&A, 10, 159